

# Chapter 3

## Rayleigh-Taylor instabilities with anisotropic lithospheric viscosity

### 3.1 Abstract

Rocks often develop fabric when subject to deformation, and this fabric causes anisotropy of physical properties such as viscosity and seismic velocities. We employ two-dimensional analytical solutions and numerical flow models to investigate the effect of anisotropic viscosity on the development of Rayleigh-Taylor instabilities, a process strongly connected to lithospheric instabilities. Our results demonstrate a dramatic effect of anisotropic viscosity on the development of instabilities - their timing, location, and, most notably, their wavelength are strongly affected by the initial fabric. Specifically, we find a significant increase in the wavelength of instability in the presence of anisotropic viscosity which favors horizontal shear. We also find that an interplay between regions with different initial fabric gives rise to striking irregularities in the downwellings. Our study shows that for investigations of lithospheric instabilities, and likely of other mantle processes, the approximation of isotropic viscosity may not be adequate, and that anisotropic viscosity should be included.

---

<sup>0</sup>Published as: Lev, E. and B.H. Hager, Rayleigh-Taylor Instabilities with anisotropy lithospheric viscosity, *Geophys. J. Int.* 173 (2008), p. 806-814.

## 3.2 Introduction

The response of anisotropic materials to stress depends on the orientation of the stress relative to the orientation of the anisotropy. Anisotropy of seismic wave speed in rocks has been studied vigorously in the last decades, both in experimental (e.g. Zhang and Karato, 1995) and theoretical work (e.g. Kaminski and Ribe, 2001). It has been shown that the deformation of rocks and minerals leads to development of crystallographic preferred orientation (CPO), which leads to seismic anisotropy (Karato et al., 1998). In addition, rotation of grains and inclusions, alignment of micro-cracks or melt lenses, and layering of different phases all lead to the development of shape preferred orientation (SPO), an important source for seismic anisotropy (e.g. Crampin, 1978; Holtzman et al., 2003; Maupin et al., 2005).

The anisotropic viscosity (AV) of earth materials has received less attention, but its effects are dramatic. Using laboratory experiments, Durham and Goetze (1977) showed that the strain rate of creeping olivine with preexisting fabric depends on the orientation of the sample and can vary by up to a factor of 50. This is because the orientation of the sample relative to the applied stress determines which slip systems are activated. In the experiments of Bai and Kohlstedt (1992) on high-temperature creep of olivine and those of Wendt et al. (1998) on peridotites, the measured strain rate depended strongly on the relative orientation of the applied stress to the sample crystallographic axis. Honda (1986) calculated the long-wavelength constitutive relations for a transversely isotropic material, and concluded that these can be characterized by two viscosities - a normal viscosity ( $\eta_N$ ), associated with principal stresses normal to the easy-shear planes, and a shear viscosity ( $\eta_S$ ), associated with shearing parallel to the easy-shear planes. More theoretical work (e.g. Weijermars, 1992; Mandal et al., 2000; Treagus, 2003) was done to assess the AV of composite materials, depending on the geometry and the relative strength of each component. These studies imply that regions of the earth that are not likely to become anisotropic by means of dislocation creep and LPO development may exhibit AV due to the deformation of composite materials, such as most natural rocks, and two-phase materials, such as partially-molten rocks. Recently, Pouilloux et al. (2007) discussed the anisotropic rheology of cubic materials and the consequences for geologic materials.

A few geodynamical studies have examined the effect of AV on mantle flow. Richter and Daly (1978) and Saito and Abe (1984) used analytical solution methods to investigate the development of Rayleigh-Bénard instabilities in a viscously anisotropic medium with specified easy-shear geometry, and found a connection between the anisotropy of the fluid and the length-scales of the convection cells. In a very instructive study a few years later, Christensen (1987) showed that the inclusion of AV affects two important mantle flows - postglacial rebound and thermal convection. For example, Christensen (1987) pointed out a spatial offset between mass anomalies and the resulting geoid signal in the presence of AV, which may help to reconcile the argued mismatch between observed uplift history near ice sheet margins and models of strong viscosity stratification in the mantle. AV also leads to channeling of flow into low viscosity region such as hot rising plumes. Nonetheless, Christensen concluded that the actual effect of AV in the earth's mantle would be much smaller, as the fabric required for creating AV would be obliterated by the highly time-dependent flow. However, the abundant evidence for seismic anisotropy in the earth and its strong correlation with tectonic processes and features suggest that large parts of the mantle maintain fabric for long times. Pre-existing mechanical anisotropy in the lithosphere was shown to have an effect in various tectonic settings such as oceanic shear zones (Michibayashi and Mainprice, 2004) and continental break-up parallel to ancient orogens (Vauchez et al., 1998).

Recently, Moresi, Mühlhaus and co-workers (e.g. Moresi et al., 2002, 2003) presented an efficient algorithm for including an AV that evolves with the flow in geodynamical models. They demonstrated the new algorithm in a series of papers, looking at various geological problems, including folding of a layered medium and thermal convection. We employ this technique here to investigate lithospheric instabilities in the presence of AV.

The lithosphere is often identified as the cold upper thermal boundary layer of Earth's convecting mantle. The colder temperature of the lithosphere makes it more dense than the asthenosphere underneath, and leads to an unstable density layering (Houseman et al., 1981). This density instability may be further enhanced by thickening of the lithosphere due to convergence (Molnar et al., 1998) or emplacement of dense material (eclogite) at

the base of the lithosphere (Elkins-Tanton and Hager, 2000). Lithospheric instabilities and removal of the lower lithosphere have been invoked to explain observations in the New England Appalachians (Robinson, 1993), the Canadian Appalachians (Murphy et al., 1999), Europe (Wenzel et al., 1997), Argentina (Kay et al., 1994), the North China craton (Fan et al., 2000; Wu et al., 2005) and Tibet (England and Houseman, 1989). Regions of high seismic velocity underneath southern California (Humphreys and Clayton, 1990; Kohler, 1999; Yang and Forsyth, 2006) are also interpreted as cold material sinking from the bottom of the lithosphere, probably as part of three-dimensional small-scale convection in the region (Humphreys and Hager, 1990) or Rayleigh-Taylor instabilities (Billen and Houseman, 2004). Upwelling of hot asthenospheric material following removal of the lower lithosphere has been suggested to explain, for instance, the massive flood basalts in Siberia (Elkins-Tanton and Hager, 2000).

The removal of the bottom of the lithosphere due to a density instability can be approximated as a Rayleigh-Taylor instability (Conrad and Molnar, 1997). Previous studies of Rayleigh-Taylor instabilities addressed the effect of the density structure, the wavelength of the density perturbation between the layers, and the rheology of the layers, on the timing and location of instability onset (e.g. Whitehead, 1986; Conrad and Molnar, 1999; Houseman and Molnar, 1997; Billen and Houseman, 2004). Here we demonstrate the significance of pre-existing and evolving fabric.

### 3.3 Anisotropic viscosity and the wavelength of instabilities

We begin our investigation with a simple conceptual setup: a dense anisotropic layer laying over a more buoyant isotropic half-space. All of the models in this study are two-dimensional. The interface between the two layers is perturbed by a small initial displacement  $w(x) = w_0 \cos(kx)$ , where  $x$  is the horizontal direction, and  $k$  is the wave number of the interface perturbation. Our goal in this section is to examine the dependence of the growth rate of instabilities on the wave number of the perturbation, the initial orientation - horizontal or

dipping - of the easy-shear planes, and the ratio between the shear and normal viscosities. We use both an analytical solution and numerical experiments for this purpose.

### 3.3.1 Governing equations

We treat the mantle as an incompressible fluid, an approximation valid for slow viscous deformation in the upper mantle (e.g. Schubert et al., 2001). The main equation to be solved is conservation of momentum:

$$\frac{\partial \sigma_{ij}}{\partial x_j} - \frac{\partial p}{\partial x_i} + f_i = 0 \quad (3.1)$$

where  $\sigma_{ij}$  is the deviatoric stress tensor,  $p$  is the pressure,  $f_i$  is the force acting in the  $i$ -th direction, and inertia is neglected. For our case,  $f_z = \rho g \hat{z}$ , where  $z$  is the vertical coordinate.

The flow also has to fulfill the continuity requirement for an incompressible material:

$$\frac{\partial v_i}{\partial x_i} = 0 \quad (3.2)$$

where  $\mathbf{v}$  is the velocity.

A central equation for any flow model is the constitutive law, relating stress and strain in the system. The constitutive law we use in this study reflects the anisotropic rheology of the materials. The simplest form of anisotropy is transverse isotropy (TI), as for a deck of cards. As shown by Honda (1986), a TI material can be characterized by two viscosities - a normal viscosity,  $\eta_N$ , and a shear viscosity,  $\eta_S$ . This form of anisotropy can describe both a layered medium, consisting of layers of different strength, or the crystallographic preferred orientation of anisotropic minerals with a dominant easy glide plane. The normal viscosity governs deformation when the two principle stresses are oriented normal and parallel to the glide plane, while the shear viscosity governs deformation when the principle stresses are oriented at  $45^\circ$  to the glide plane. The exact expressions we use for our analysis are given in equations (3.4) and (A1).

We note that in this formulation, materials with horizontal and vertical easy-shear directions are mathematically equivalent. This is similar to a stack of books on a shelf - it is easy

to shear the stack horizontally both when the books stand up (vertical easy-shear planes) and when they lay on top each other (horizontal easy-shear planes). We thus examine two end-member setups - in one the anisotropic dense layer initially has a horizontal easy-shear direction, and in the other the easy shear direction initially dips at  $45^\circ$ .

### 3.3.2 Analytical solution

In this analysis we use the propagator matrix technique (e.g. Hager and O’Connell, 1981) to calculate the growth rate of the instabilities as a function of the wavelength of a small perturbation in the interface between the two materials. The mean depth of the interface is at  $z = 0$ . The boundary conditions for our problem are no-slip at the top boundary ( $z = 1$ ), which we take to be the base of the rigid part of the lithosphere, and vanishing of the velocities and stresses as  $z \rightarrow -\infty$ . By calculating the vertical velocity  $v(z = 0)$  we are able to track the change in position of the boundary. The derivation is outlined in Appendix A, and an important outcome of it is that

$$v(z = 0) \equiv \frac{\partial w}{\partial t} \propto w \quad (3.3)$$

Because the velocity of the interface is proportional to the amplitude of the boundary topography (eqn. 3.3), the change in the interface depth follows an exponential growth rule:  $w(z, t) = e^{\frac{t}{\tau}}$ .  $\tau$ , the growth rate, is a function of the wave number  $k$  of the perturbation  $w$ , and of the two viscosities  $\eta_N$  and  $\eta_S$ .

The results we present in section 3.3.4, as well as Appendix A, give insight into the relationship between the growth rate and a range of viscosities and wave numbers. We note here that this analysis is valid only for small interface perturbations, so we can assume that the orientation of the AV does not evolve.

### 3.3.3 Numerical experiments

To follow the instability to finite amplitude requires a numerical approach. We solve the flow equations using a finite element formulation on an Eulerian mesh embedded with Lagrangian

integration-points (“particles”), as described by Moresi et al. (2003). In this method, particles carry the material properties, and foremost their deformation history and the derived AV. Variables such as velocity and pressure are calculated at the location of the mesh nodes, which are fixed in space. We use the software package *Underworld* (Moresi et al., 2007) to solve the flow equations.

### Including anisotropy in the flow equations

To include AV in our numerical experiments, we use the particle-in-cell formulation (Moresi et al., 2003). By this method, the anisotropy is represented by a set of *directors* advected through the model, analogous to particles (Mühlhaus et al., 2002b). The directors are vector-particles pointing normal to the easy-glide plane or layer, thus defining the directions associated with  $\eta_N$  and  $\eta_s$ . In each time step of the calculation, the directors are advected and rotated by the flow, and in return determine the viscosity structure for the next time step (Mühlhaus et al., 2004).

The AV enters the equation of momentum through a ‘correction’ term added to the isotropic part of the constitutive equation relating stress and strain rate (Mühlhaus et al., 2002b):

$$\sigma_{ij} = -p\delta_{ij} + 2\eta_N\dot{\epsilon}_{ij} - 2(\eta_N - \eta_S)\Lambda_{ijkl}\dot{\epsilon}_{kl} \quad (3.4)$$

where  $\eta_N, \eta_S$  are the normal and shear viscosities, respectively,  $\sigma$  is the deviatoric stress tensor, and  $\dot{\epsilon}$  is the strain rate tensor.  $\Lambda$  reflects the orientation of the directors in space, denoted by  $\mathbf{n}$ :

$$\Lambda_{ijkl} = \frac{1}{2}(n_i n_k \delta_{lj} + n_j n_k \delta_{il} + n_i n_l \delta_{kj} + n_j n_l \delta_{ik}) - 2n_i n_j n_k n_l \quad (3.5)$$

The evolution of the orientation of directors in time is controlled by integration over time of

$$\dot{n}_i = -\frac{\partial v_i}{\partial x_j} n_j \quad (3.6)$$

(Belytschko et al., 2001). A more detailed description of how the anisotropy described by

the directors enters the equations of flow and how it is represented in the finite element formulation is given by Mühlhaus et al. (2002b).

## Model setup

We carried out a suite of two-dimensional numerical experiments to investigate the development of instabilities in the presence of AV. The numerical models we use in this section consist of a dense layer with a uniform fabric throughout its width, overlying a more buoyant layer. The model domain is a rectangular box with an aspect ratio of 1:6.4, comprised of 240x32 elements. We place a dense layer in the top 15% of the box. Because the thickness of the lower layer is much greater than that of the upper layer, our analytical solution for a layer overlying a half-space should provide a reasonable approximation to the finite-depth domain. The interface between the layers is a cosine curve with an initial amplitude of 0.01. We compare the growth rate for models with an either horizontal or dipping initial easy-shear direction for a range of interface perturbation wavelengths. We measure the non-dimensional time that it takes to displace the interface by one element length, and define this time as the reciprocal of the growth rate. The ratio of the shear viscosity to the normal viscosity for the anisotropic material is 0.1 in all cases, in accordance with the theoretical estimations of Mandal et al. (2000) and Treagus (2003) and within the range of values measured in the experiments of Durham and Goetze (1977). The isotropic viscosity of the buoyant lower layer is equal to the normal viscosity ( $\eta_N$ ) of the dense layer.

### 3.3.4 Results - a homogeneous but anisotropic upper layer

Both our numerical experiments and our analytical solution predict that the most unstable wavelength for a dense layer with a horizontal fabric is much longer than that for an isotropic layer or for a layer with a dipping fabric. From our analytical solution, we calculate the normalized values of  $\tau$  for a range of wave-numbers and viscosity ratios, for both a horizontal fabric and a dipping fabric. The results are plotted in figure 3-1. For comparison, we also plot the growth-rate curves for models with an isotropic dense layer with a viscosity that equals the geometric and the arithmetic averages of the shear and normal viscosities of the

anisotropic material. Figure 3-1 clearly shows that the effect of anisotropy is dramatic, especially for a material with initially horizontal easy-shear direction. For such a fabric, the minimum point of the growth rate curve, which determines the most unstable wavelength, shifts to a longer wavelength as the viscosity ratio becomes smaller (blue curves in figure 3-1). For a case of a shear viscosity that is 10 times smaller than the normal viscosity, a fairly conservative estimate, the most unstable wavelength is twice as long as for the isotropic one; For  $\eta_S/\eta_N = 0.01$ , the increase is by a factor of 3.5. This increase in the most unstable wavelength is comparable to the effect of having an isotropic dense layer with a lower viscosity (green curves in figure 3-1). Also, the shape of the curve is changed compared to the isotropic case, and becomes flatter. For a dipping fabric (figure 3-1, red curves), the change is minor - the most unstable wavelength is equal to the isotropic and isoviscous one, and for long wavelengths the stability curves are almost identical for all degrees of anisotropy.

Figure 3-2 shows the results from our numerical experiments. We plot the growth rate versus the wave number of the density perturbation for each initial configuration of the dense anisotropic layer: horizontal fabric (blue line, squares), 45°-dipping fabric (red line, diamonds) and isotropic (black line, circles). The results agree with the predictions from the analytical solution presented above - the fastest growth rate for the horizontal fabric is at a longer wavelength than that for the dipping fabric or for an isotropic layer, and the curve is indeed flatter at longer wavelengths. The minimum growth rate for a dipping fabric is at almost the same wavelength as that for an isotropic material, again in agreement with the analytical predictions. Figure 3-3 shows the material distribution in the different model configurations after the fastest drips have sunk half of the box depth, as well as the approximate location of the initial perturbed interface (yellow curve). These snapshots demonstrate clearly that the wavelength of the instabilities developing in the initially horizontal models is greater than of those developing in the initially-dipping models. This emphasizes the advantage gained by using numerical experiments - the analytical solution gives insight into the behavior of instabilities at small amplitudes, while the numerical experiments are essential for predicting the behavior as the flow progresses and instabilities of finite-amplitude develop.

## 3.4 Laterally-varying anisotropy

Intrigued by the dramatic results for a simple model of a homogeneous anisotropic dense layer described above, we proceed and use numerical experiments to examine the effect of including lateral variations in the initial anisotropic fabric of the dense layer.

### 3.4.1 Model setup

Figure 3-4 depicts the model geometry and initial and boundary conditions. The model domain is again a rectangular box with an aspect ratio of 1:6.4. The location and amplitude of the interface between the layers is the same as in section 3.3. Following the findings of section 3.3, we perturb the interface with a wavelength long enough to allow deformation at a wide range of wavelengths to develop freely. The dense layer now contains two anisotropic regions in the center, each 1.6 wide, and two isotropic regions of the same high density near the edges. The anisotropic regions differ only by their initial fabric orientation - one (shown in red) initially has a horizontal easy shear direction, and the other has an easy shear direction initially dipping at  $45^\circ$  (shown in yellow). The viscosity of the buoyant layer is equal to the normal viscosity of the anisotropic layer. The shear viscosity of the anisotropic material is a factor of 10 less than its normal viscosity. We shift the anisotropic regions laterally in different models in order to change the phase between the viscosity structure and the density interface perturbation. We then examine the development of drips for each configuration.

### 3.4.2 Results - a heterogeneous upper layer

In figure 3-5 we show the instabilities that develop in our models. The different panels depict models with different configurations of the initial fabric domains, shown in red and yellow, as well as the results for an isotropic model for comparison (Fig. 3-5a). We also show the trace of the original density interface between the dense lithosphere and the underlying mantle (black horizontal curve) and the location of the deepest points of the initial perturbation of the density interface (dashed vertical lines).

Several first-order observations can be made in figure 3-5. First, there is a striking difference between the instabilities that develop in the two anisotropic domains. Most notably, the wavelengths of the downwellings that develop in the domain with easy horizontal shear are much longer than the wavelengths in the dipping-fabric domains or in the isotropic model (Fig. 3-5a). In addition, the domain which starts with easy horizontal shear (red) develops instabilities faster than the domain which starts with easy shear direction dipping at  $45^\circ$  (yellow). Next, for several situations, the fastest-growing downwelling does not coincide with the locations of maximum thickness of the dense layer, but is offset horizontally by up to 0.5 of the box depth (Fig. 3-5b,g). Finally, almost all of the fastest-growing instabilities occur near the edges of the domain of horizontal easy shear (excluding the case where the thickest part of the dense layer was exactly in the center of the domain of initial horizontal anisotropy), but the instabilities that develop in the dipping easy shear domain develop in its interior. Evidently, the initial fabric and its lateral variations influence the flow significantly.

### 3.5 Discussion

Our models are set up in a non-dimensional manner, for generality. It is interesting, though, to re-scale the results to lithospheric dimensions. The dense layer (top 15% of the box) corresponds to the viscously-mobile part of the lithosphere, which is approximately its lowest 40 km. The viscosity of the lithosphere is temperature-dependent, and is believed to decrease exponentially with depth, with a reasonable decay length of about 10 km (Molnar et al., 1998). If we take the viscosity at the base of the lithosphere to be  $10^{19}$  Pa s (Hager, 1991), then the average viscosity for a 40 km thick layer, calculated as  $\langle \eta \rangle = \exp(\frac{\log \eta_1 + \log \eta_2}{2})$ , is  $7.4 \cdot 10^{19}$  Pa s. Using the thickness of the lower lithosphere as the characteristic length scale, we can estimate the spacing between the isotropic instabilities as 130 km, and the wavelength of the longest anisotropic instabilities is close to 400 km. The lateral offset between the downwellings and the locations of maximum lithospheric thickness scales to a maximum of approximately 150 km. We re-scale velocities based on the the viscosity and density contrast, using the ‘‘Stokes Velocity’’ ( $V_{Stokes} = \frac{\Delta\rho * g * h^2}{\eta}$ , where  $\eta$  is the effective

viscosity of the dense layer,  $\Delta\rho$  is the density contrast and  $h$  is the dense layer thickness). We estimate the difference between the density of the lower lithosphere and the density of the underlying asthenosphere as  $40 \text{ kg/m}^3$  (Molnar et al., 1998). After substituting the above values we can now calculate the scaling of time. We estimate that the time it takes for the drips to sink to a depth of 160 km (the stage shown in Fig. 3-5) is approximately 12 Myrs. This duration is within the range of times estimated by Houseman and Molnar (1997) for removal of the base of an unstable thickened lithosphere. This time and distance of sinking imply an average sinking velocity of 14 mm/yr.

The models we present here are a preliminary attempt at this problem, and thus have some shortcomings when compared with the lithosphere. First, the fabric development rule we use is a simple rotational evolution law, and does not take into account factors such as temperature, strain rate, and recrystallization, all known to affect the development of CPO in rocks. Second, the rheology we use is a Newtonian creep law, while in fact anisotropy due to CPO requires deformation in the dislocation creep regime, which is a power-law creep process. Additionally, all our experiments are carried out in two dimensions. There may be interesting consequences when these effects are studied in a three-dimensional setup, especially given the three-dimensional nature of some observed mantle instabilities (e.g. Yang and Forsyth, 2006). A three-dimensional model would also be able to include orthorhombic symmetry and would not be constrained to the use of transverse isotropy. Hopefully future work would be able to assess the significance of these factors and their implications.

Both our analytical solution and the numerical flow models predict that the wavelength of Rayleigh-Taylor instabilities would be longer for an anisotropic material, most significantly for a fabric favoring horizontal flow. Some intuitive understanding of this can be gained if we imagine a horizontally layered medium - it is much easier for such a medium to flow sideways by simple shear, and not to develop vertical drips. Drips will eventually develop in locations where the horizontal flow encounters resistance - for instance in the form of a domain with a different fabric. This is likely the reason that the largest downwellings developed in the edges of the domains with initial horizontal easy shear direction (red domains in Fig. 3-5). If, on the other hand, the initial fabric is at an angle to the main acting force, it will be easier for

the instabilities to thicken by pure shear and ‘break’ the layering structure, and hence will be more likely to follow a wavelength closer to the isotropic one. This result is in agreement with the experiments of Richter and Daly (1978), who found that anisotropy leads, in general, to longer wavelengths of instabilities. Saito and Abe (1984) performed a marginal stability analysis for a related model setup (bottom-heated Rayleigh-Bénard convection with stress free boundaries and horizontal layering) and, similarly to our results, found that the stability curves flatten out and that the minimum shifts to a longer wavelength with lower viscosity ratio.

We emphasize at this point that numerical techniques such as the one we use here have several important advantages. Analytical solutions, while elegant, give insight into the behavior of instabilities only at small amplitudes, and thus numerical experiments are essential for predicting the flow as it progresses and instabilities of finite-amplitude develop. Additionally, the numerical technique we use is capable of modeling flows in which the fabric is evolving and the orientation of the anisotropy is not fixed in space, as opposed to the situation in our, as well as earlier (e.g. Richter and Daly, 1978; Honda, 1986), analytical solutions. It is also straightforward to include lateral variations of the anisotropy, a scenario highly relevant to tectonic processes in natural environments.

The strong effect of pre-existing fabric on the development of Rayleigh-Taylor instabilities may have important implications for the stability of the lithosphere. In our models, the fastest growing downwelling sometimes develops away from the initially deepest region of the density interface, due to the interaction between domains with different fabric orientation. This change in geometry may provide a simple explanation for the offset of the mantle drip beneath the Sierras (e.g. Saleeby and Forster, 2004). Our findings of the effect of AV on the wavelength of instabilities should also be considered in the context of other locations, for example Tibet. Conrad and Molnar (1997) argued that the wavelength of Rayleigh-Taylor instabilities predicted to arise from the collision between India and Eurasia is much shorter than the wavelength of the Tibetan plateau, and hence such instabilities are unlikely to be the cause of the rapid uplift of the plateau at 5-10 Myrs ago. If, however, the existing fabric in the collision zone was such that it leads to longer wavelengths, this possibility may need

to be reconsidered.

The points of contact between regions with different existing fabric appear to have unique significance. This hints that when tectonic units which have gone through a different evolution and developed different fabric are juxtaposed, this contact point may be particularly unstable. An example of such a situation may be the placing of a spreading center, which is characterized by horizontal easy-shear planes, next to a region that is more horizontally-resistant. When this combination is put under compression, the horizontal easy shear planes will be unstable at the contact point, which may lead to initiation of downwelling and perhaps even subduction. Subduction initiation at extinct spreading centers is likely the explanation for the subduction zone at the Macquarie region south of New-Zealand (Lebrun et al., 2003) and near the Oman ophiolite (Michibayashi and Mainprice, 2004). Our results clearly show that additional knowledge of the anisotropic fabric of the lithosphere, and, specifically, the orientation of dipping fabrics, can shed light on different tectonic problems, and highlights the importance of overcoming the difficulties in making such measurements (e.g. Chevrot and van der Hilst, 2003).

### **3.6 Summary**

We show the dramatic effect of anisotropic viscosity on the development of Rayleigh-Taylor instabilities. The wavelength, timing and shape of the instabilities that develop in our models are strongly affected by the initial fabric prescribed. The most notable effect of anisotropic viscosity on Rayleigh-Taylor instabilities, demonstrated here both analytically and numerically, is the shift to longer wavelengths when the initial fabric of the dense material favors horizontal flow (horizontal or vertical fabric). The interplay between regions with different orientations of initial fabric gives rise to a variety of features, such as an offset of the main downwellings away from the deepest point of the perturbed interface, and demonstrates the importance of considering the deformation history of all the units participating in a tectonic setting. Our results show that for the study of lithospheric instabilities, and likely of other mantle processes, the common isotropic approximation may not be accurate, and

hence anisotropic viscosity should be included.

**Acknowledgements.** We are grateful for helpful discussions with Linda Elkins-Tanton, Ming Fang, Greg Hirth, Eduard Kaminski, Laurent Pouilloux, and Andrea Tommasi. A thoughtful review by Gregory Houseman helped greatly to improve this manuscript. The research presented here was supported by NSF under grants EAR-0337697 and EAR-0409564

### 3.7 Appendix A: Derivation of analytical solution

We begin by defining the following anisotropic constitutive relations, which describe a transversely isotropic (TI) material in the two special cases considered here of 1) easy-shear on horizontal/vertical planes and 2) easy-shear on planes dipping at  $45^\circ$ :

$$\sigma_{xx} = 2\eta_{ps}\dot{\epsilon}_{xx} \quad (\text{A1a})$$

$$\sigma_{zz} = 2\eta_{ps}\dot{\epsilon}_{zz} \quad (\text{A1b})$$

$$\sigma_{xz} = \eta_{ss}\dot{\epsilon}_{xz} \quad (\text{A1c})$$

where  $\eta_{ps}$  is a viscosity corresponding to pure shear stresses, and  $\eta_{ss}$  corresponding to simple-shear. For a material with a horizontal easy-shear direction (horizontal layering, for instance)  $\eta_{ss}$  is equivalent to  $\eta_S$  defined in section 3.3.1,  $\eta_{ps} \equiv \eta_N$ , and  $\eta_{ss} < \eta_{ps}$ . For an anisotropic material with a dipping easy-shear direction,  $\eta_S \equiv \eta_{ps} < \eta_{ss} \equiv \eta_N$ . For an isotropic material,  $\eta_{ps} = \eta_{ss}$ . This constitutive relation can be derived from a matrix form similar to that in equation 3.4:  $\sigma_{ij} = 2\eta_N\epsilon_{ij} - 2(\eta_N - \eta_S)\Lambda_{ijkl}\epsilon_{kl}$  where  $\Lambda$  is an alignment tensor reflecting the orientation of the symmetry axis. Then, the transformation from a horizontal symmetry anisotropy to a dipping symmetry can be achieved by a rotation of the 4th-order tensor  $\Lambda$ .

In our analytical solution, we employ the propagator matrix technique (e.g. Hager and O'Connell, 1981) to calculate the growth rate of Rayleigh-Taylor instabilities as a function of the wavelength of the density perturbation between the two materials. We set  $z = 0$  at the interface between the layers,  $z = 1$  at the top of the dense layer, and the initial location of the density interface as  $w = w_0 \cos(kx)$ . For the horizontal and  $45^\circ$ -dipping orientations we consider here, this definition of the interface perturbation leads to  $v_x, \sigma_{zz} \propto \cos(kx)$ , and  $v_z, \sigma_{xz} \propto \sin(kx)$ , where  $k$  is the wave number. For other orientations there may be a phase shift with depth (Christensen, 1987). Thanks to the orthogonality of the trigonometric basis functions, we can write a simplified set of equations for each wave number. We define a vector  $\mathbf{u} = [v, u, \sigma_{zz}, \sigma_{xz}]$ , where  $v$  is the vertical velocity,  $u$  is the horizontal velocity,  $\sigma_{zz}$  is the normal stress in the  $z$  direction,  $\sigma_{xz}$  is the shear stress, and  $x$  and  $z$  are the horizontal

and vertical coordinates. After some manipulation, this definition of  $\mathbf{u}$  enables us to express the equations of flow in each layer for every  $k$  as

$$D\mathbf{u} = \mathbf{A}\mathbf{u} + \mathbf{b} \quad (\text{A2})$$

where  $D = \frac{\partial}{\partial z}$ , and  $\mathbf{b}$  is a forcing term. The matrix  $\mathbf{A}$  is where the anisotropic viscosity is manifested.

The definition of the anisotropic constitutive relation above leads to a matrix  $\mathbf{A}$  of the form:

$$\mathbf{A} = \begin{bmatrix} 0 & -k & 0 & 0 \\ k & 0 & 0 & \eta_{ss}^{-1} \\ 0 & 0 & 0 & -k \\ 0 & 4\eta_{ps}k^2 & k & 0 \end{bmatrix} \quad (\text{A3})$$

When  $\eta_{ps} = \eta_{ss}$  (isotropic material), the expression in (A3) is equal to the matrix  $\mathbf{A}$  given by Hager and O'Connell (1981). Otherwise, it reflects the anisotropic viscosity of the material by including the two different viscosities.

The solution to equation (A2) is of the form

$$\mathbf{u}(z) = e^{\mathbf{A}(z-z_0)}\mathbf{u}(z_0) + \int_{z_0}^z e^{\mathbf{A}(z-\xi)}\mathbf{b}(\xi)d\xi \quad (\text{A4})$$

We define the propagator matrix  $\mathbf{P}(z, z_0) = e^{\mathbf{A}(z-z_0)}$ , so that the velocities and stresses can be expressed as

$$\mathbf{u}(z) = P(z, z_0)\mathbf{u}(z_0) + \sum_{i=1}^n P(z, \xi_i)\mathbf{b}(\xi_i)\Delta\xi_i \quad (\text{A5})$$

where  $\xi_i$  is the depth at the center of a the  $i$ -th layer and  $\Delta\xi_i$  is the layer thickness. The propagator matrix for an anisotropic material will naturally be different than the propagator matrix for an isotropic material, given the difference in the corresponding  $\mathbf{A}$  matrices. The boundary conditions for our problem are no-slip at the top boundary ( $z = 1$ ), which we take to be the base of the rigid part of the lithosphere, and vanishing of the velocities and stresses

as  $z \rightarrow -\infty$ . We can express the boundary conditions using the vector  $\mathbf{u}$  defined earlier:

$$\mathbf{u}(z = 1) = [0, 0, \sigma_{zz}^t, \sigma_{xz}^t], \quad \mathbf{u}(z = -\infty) = [0, 0, 0, 0] \quad (\text{A6})$$

In order to fulfill the boundary condition as  $z \rightarrow -\infty$ ,  $\mathbf{u}$  just below the interface has to be of the form  $\mathbf{u}(z = 0^-) = [C_1/2k, C_2/2k, C_1, C_2]$ , where  $C_1, C_2$  are the  $\sigma_{zz}$  and  $\sigma_{xz}$  at the interface. We add a normalized forcing term which here represents the gravitational forcing in the  $z$  direction. Thus  $\mathbf{u}$  across the interface, at the bottom of the dense layer, becomes  $\mathbf{u}(z = 0^+) = [C_1/2k, C_2/2k, C_1 + 1, C_2]$ . We propagate this  $\mathbf{u}(z = 0^+)$  upwards to the top interface using the anisotropic propagator matrix  $P_{ani}$ :  $\mathbf{u}(z = 1) = P_{ani}\mathbf{u}(z = 0^+)$ . From the no-slip boundary condition at the top, the first two components of the resulting vector are equal to zero. We now have two equations and two unknowns -  $C_1$  and  $C_2$ . We solve for these two unknowns and use the result to calculate the vertical velocity at the interface.

The change in the interface location with time is equal to the vertical velocity at the interface -  $v(z = 0)$ , where  $v$  is the vertical velocity. A result of the derivation described above is that the vertical velocity at the interface is proportional to the perturbation of the interface, that is:

$$v(z = 0) \equiv \frac{\partial w}{\partial t} \propto w \quad (\text{A7})$$

Therefore the change in the interface depth follows an exponential growth rule:  $w(z, t) = e^{\frac{t}{\tau}}$ , which gives the dependence of the growth rate  $\tau$  on the model parameters:

$$\tau = \frac{1}{K(\eta_{ps}, \eta_{ss}, k)} \quad (\text{A8})$$

$K$  is a complicated function of the viscosities and the wave number, of the form  $\Delta\rho g \times [a \text{ sum of exponents of powers of } \eta_N, \eta_s, \text{ and } k]$ . The exact expression is too long to give here explicitly, but can be obtained using the Matlab code in the electronic supplement. The resulting relationship between  $1/K$  ( $\tau$ ) for a range of wave numbers and a set of viscosity ratios is demonstrated in figure 3-1; Figure S1 (Electronic Supplement) shows a similar calculation for a range of viscosity ratios and  $k = 0.1$ .

A careful inspection of the anisotropic matrix  $A_{ani}$  and the anisotropic propagator matrix  $P_{ani}$  reveals a very interesting phenomenon - an oscillatory behavior with depth for certain viscosity ratios. Let us define  $\delta$ , the viscosity ratio, as  $\delta = \frac{\eta_{ss}}{\eta_{ps}}$ . As we noted earlier, for a material with a horizontal easy-shear direction  $\eta_{ss} < \eta_{ps}$ , and thus  $\delta < 1$ , while for a material with a dipping easy-shear direction  $\eta_{ss} > \eta_{ps}$  and  $\delta > 1$ . The eigenvalues of the matrix  $\mathbf{A}$  are used in the expression for the propagator matrix and control the behavior of the velocities and stresses in the medium. For an isotropic material, these eigenvalues are real and repeated, and the propagator matrix includes additional terms depending linearly on the depth —  $P \propto (1 \pm kz)e^{\pm kz}$  (Hager and O’Connell, 1981). The anisotropic  $\mathbf{A}$  matrix has, on the other hand, four distinct eigenvalues, of the form:

$$\lambda_i = \pm k \left( \frac{2 - \delta \pm 2\sqrt{1 - \delta}}{\delta} \right)^{\frac{1}{2}} \quad (\text{A9})$$

All the eigenvalues for a material with horizontal fabric ( $\delta < 1$ ) are real, leading to a propagator matrix (and thus velocities and stresses) that are proportional to  $e^{\pm\lambda_i z}$ . Anisotropy with a 45° dipping easy-shear direction ( $\delta > 1$ ) implies that the four eigenvalues are complex, and thus the velocities and stresses are proportional to  $\cos(Im(\lambda_i)z)e^{\pm Re(\lambda_i)z}$  and  $\sin(Im(\lambda_i)z)e^{\pm Re(\lambda_i)z}$ . This gives rise to a non-monotonic behavior of the velocity and stress fields with depth for dipping anisotropy, plotted in Figure 3-1. This oscillatory behavior is strongly enhanced when both the dense layer and the buoyant half-space underneath have an anisotropic, dipping fabric. The growth-rate curves for this case are given in Figure A1; the non-monotonic fluctuations are obvious, especially as  $\delta$  becomes larger.

## Figures

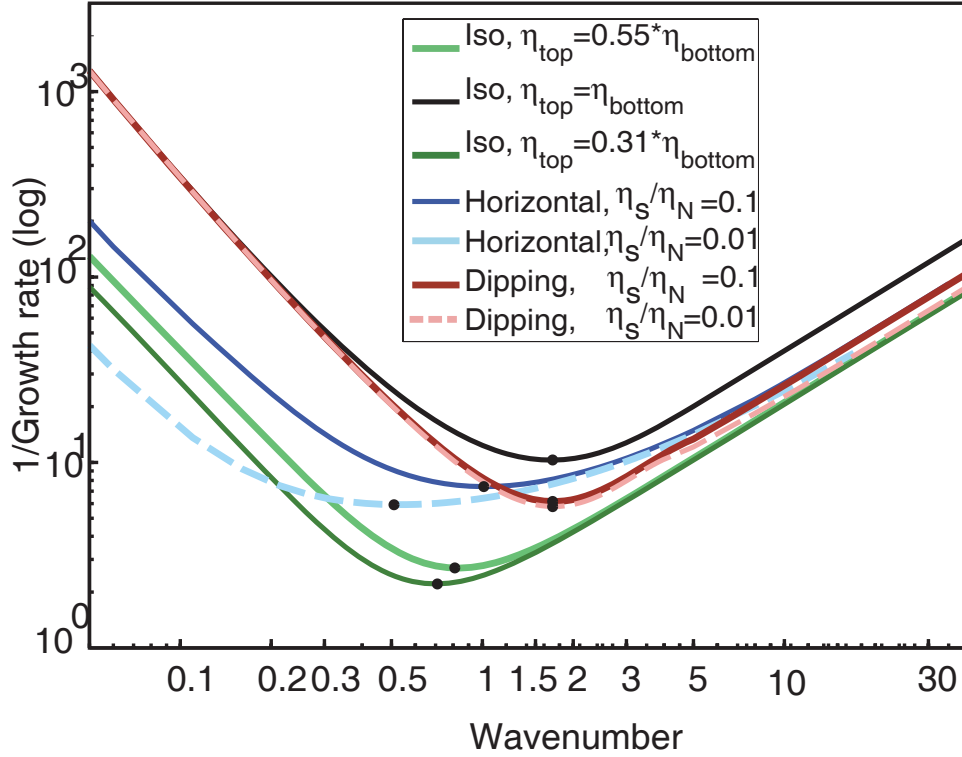


Figure 3-1: Growth-rate curves, plotting the growth rate of Rayleigh-Taylor instabilities versus the perturbation wave number, for models with varying degrees and orientations of anisotropy of a dense upper layer overlaying an isotropic half-space: black - isotropic upper layer with viscosity equal to the viscosity of the bottom half-space; green curves - isotropic dense layer with viscosity equal to the average of the normal and shear viscosities of the anisotropic cases (dark green - geometric average, light green - arithmetic average); blue curves - horizontal easy shear direction (dark blue -  $\eta_s/\eta_N = 0.1$ , dashed light blue -  $\eta_s/\eta_N = 0.01$ ); red curves - easy shear direction dipping at  $45^\circ$  (maroon -  $\eta_s/\eta_N = 0.1$ , dashed pink -  $\eta_s/\eta_N = 0.01$ ). For the anisotropic cases,  $\eta_N = \eta_{bottom}$ . The minimum point of each curve, indicating the most unstable wave number for each configuration, is also shown.

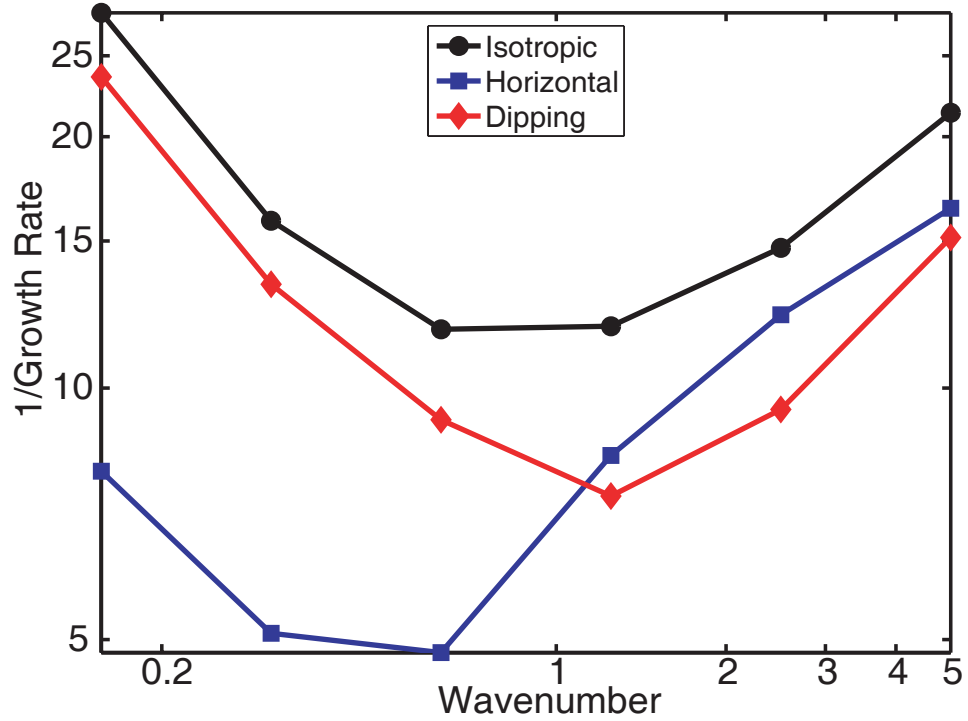


Figure 3-2: Growth-rate curves, plotting the non-dimensional growth rate versus perturbation wave number, for numerical experiments in which the anisotropic dense layer initially has a horizontal easy shear direction (blue line), a dipping easy shear direction (red line), or is isotropic (black line). The thickness of the dense layer is 0.15 of the box depth.

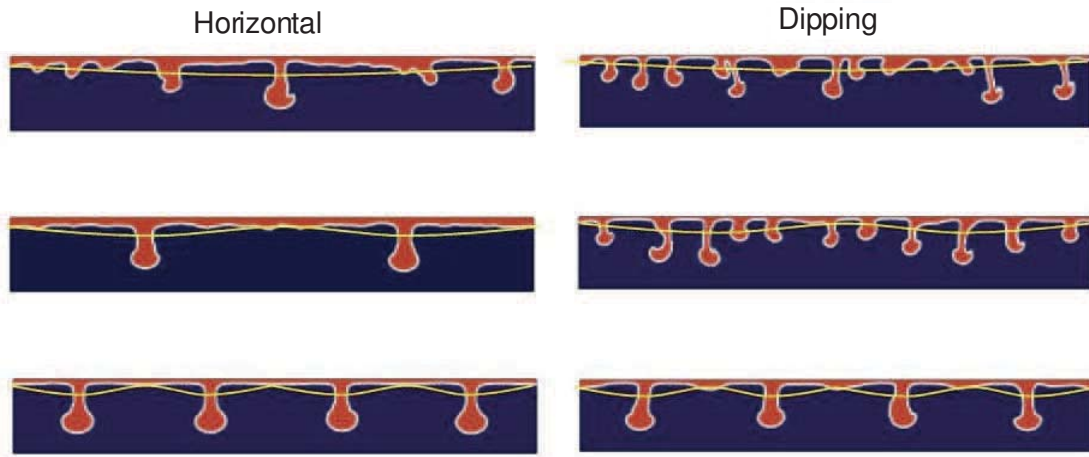


Figure 3-3: Material distribution for models with horizontal (left panels) and dipping (right panels) initial fabric of the dense top layer and various initial interface deflection wavelengths, taken after the fastest downwellings sink past half the box depth. Color denotes the materials - blue is the isotropic buoyant material and red is the anisotropic denser material. The yellow curves show the approximate location of the initial density interface, exaggerated vertically for visual clarity.

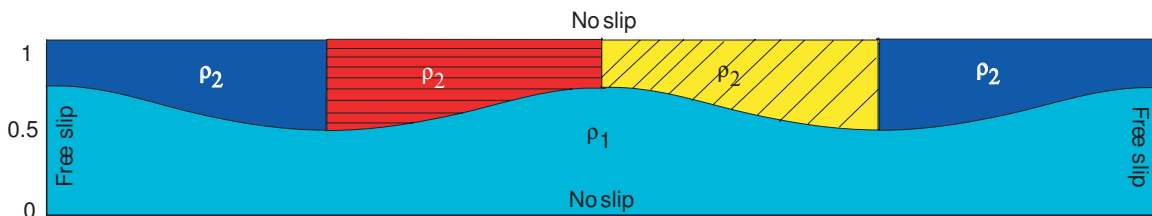


Figure 3-4: Laterally-varying anisotropy – a schematic description of the model geometry and initial conditions. The colors denote the densities and rheologies : blue - isotropic,  $\rho = 1$ ,  $\eta_{iso} = 1$ , red - anisotropic with horizontal fabric,  $\rho = 1$ ,  $\delta = 0.1$ , yellow - anisotropic with dipping fabric,  $\rho = 1$ ,  $\delta = 10$ , cyan - isotropic,  $\rho = 0$ ,  $\eta_{iso} = 1$ ). There is no slip on the top and bottom boundaries, and free slip is allowed along the side walls. The thickness of the top layer and the amplitude of the interface perturbation were exaggerated for clarity.

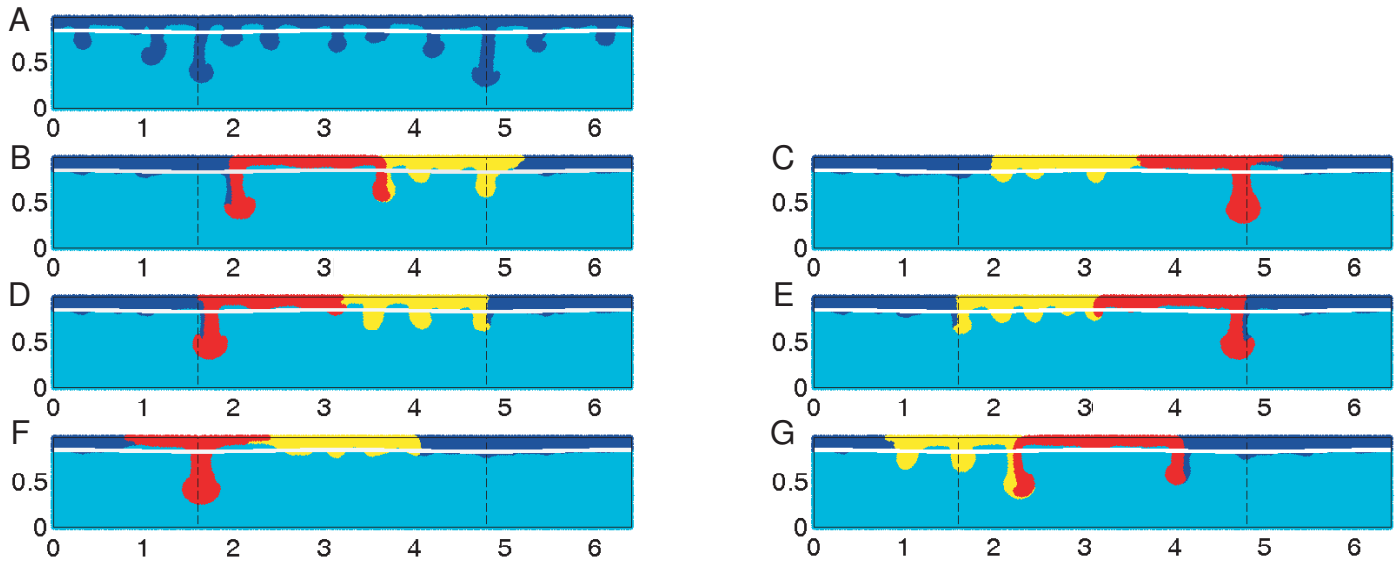
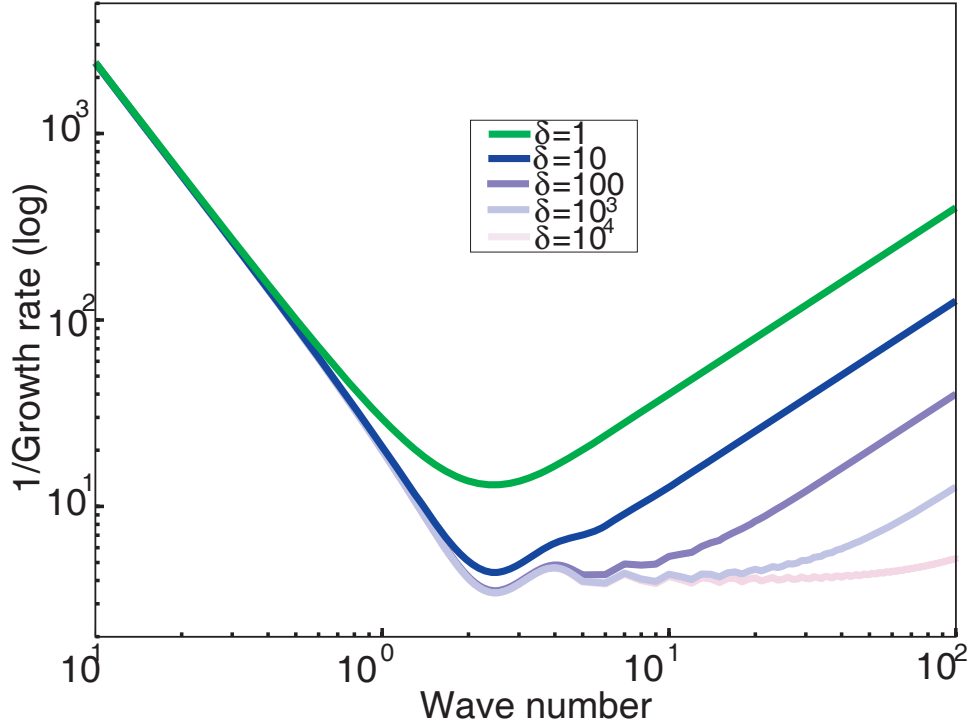


Figure 3-5: Material distribution in models with different configurations of initial anisotropic fabric taken after the fastest downwelling sinks over half the box depth. Panel A shows the results for an isotropic model. The black cosine curve at a depth of 0.15 marks the original interface between the dense and buoyant layers. The vertical dashed black lines show the deepest points of the original density interface, where the dense layer was thickest. Red material starts with a horizontal fabric; Yellow material starts with a fabric dipping at  $45^\circ$ . Blue materials are isotropic. Interestingly both panels 3-5B and 3-5G, which start with distinctly different material arrangements, show large downwellings comprised of both anisotropic materials, while others do not.



**Figure A1.**

Figure 3-1: Growth-rate curves, plotting the growth rate of Rayleigh-Taylor instabilities versus the perturbation wave number, for models of an anisotropic dense upper layer overlying an anisotropic half-space, both with a dipping easy-shear direction. The colors denote different degrees of anisotropy: green - isotropic materials; blue to pink - increasing degrees of viscosity contrast between the shear and normal viscosities. The oscillatory behavior, characteristic of materials with dipping easy-shear directions, is apparent. As the viscosity contrast increases, the curves flatten for short wavelengths.